Energy Storage Materials 8 (2017) 153–160

Contents lists available at ScienceDirect

Energy Storage Materials

journal homepage: www.elsevier.com/locate/ensm

Beaver-dam-like membrane: A robust and sulphifilic $MgBO_2(OH)$/CNT/PP nest separator in Li-S batteries

Long Kong[c,1], Hong-Jie Peng[c,1], Jia-Qi Huang[a,c,d,*], Wancheng Zhu[b,*], Ge Zhang[c], Ze-Wen Zhang[c], Pei-Yan Zhai[b,c], Panpan Sun[b], Jin Xie[c], Qiang Zhang[c,*]

[a] Advanced Research Institute for Multidisciplinary Science, Beijing Institute of Technology, Beijing 100081 China
[b] Department of Chemical Engineering, Qufu Normal University, Shandong 273165 China
[c] Beijing Key Laboratory of Green Chemical Reaction Engineering and Technology, Department of Chemical Engineering, Tsinghua University, Beijing 100084 China
[d] CAS Key Laboratory of Carbon Materials, Institute of Coal Chemistry, Chinese Academy of Sciences, Taiyuan 030001 China

ARTICLE INFO

Keywords:
Composite separator
Lithium–sulfur batteries
Magnesium borate hydroxide
Carbon
Lithium polysulfides

ABSTRACT

The assembly of various low dimensional nanomaterials into hierarchical nanostructures is a central issue since it inherits the advantages of each component and even leads to the formation of advanced materials with unforeseen properties. The rational integration of nanomaterials into an effective membrane is expected to regulate the complex energy chemistry of lithium–sulfur (Li–S) batteries. In this contribution, a bio-inspired beaver-dam-like membrane was proposed as a robust and sulphifilic nest separator for advanced Li–S cells. The nest separator was integrated by a continuous polypropylene, a highly electrical conducting network of carbon nanotubes (CNTs), and lithium polysulfide (LiPS)-suppressing adsorbents of magnesium borate hydroxide (MBOH) nanofibers to enhance the redox reaction of LiPS intermediates and retard their migration in a working cell. The kinetic behavior of LiPS conversion on sulphifilic surface was well understood through direct measurements of lithium sulfide nucleation and potentiostatic discharge profiles, demonstrating the interfacial affinity between MBOH and LiPS. The smart hybridization of MBOH and CNTs in nest separators rendered the Li–S cell with long cycling stability of 785 mA h g^{-1} after 200 cycles, high rate capability of 500 mA h g^{-1} at 6 C, enhanced areal capacity of 2.91 mA h cm^{-2}, and improved thermal stability. The presented bio-inspired design sheds fresh light on a novel electrolyte system to demonstrate the superb electrochemical performances of Li–S batteries and affords new insights into understanding the interfacial interaction between LiPS and adsorbents.

1. Introduction

The assembly of various low dimensional nanomaterials with distinct physical and chemical properties into hierarchical nanostructures is a central issue since it inherits the advantages of each component and even leads to the formation of advanced materials with unforeseen properties [1]. The rational integration of nanomaterials into a well-designed and more effective architecture with unique property and performance is still a great challenge in material science and energy storage. Inspired by numerous ingenious structures from the nature, various bio-inspired structures have been proposed as advanced functional materials [2–8].

The beaver dams are constructed by driving tree branches and logs into the mud of bed to form a base, followed by construction of the superstructure with sticks, rocks, grass, leaves, and anything else available. The integration of soft and rigid components renders the dam structural durability. The beaver dam allows the drain off excess water but effectively block rocks and branches, which can further reinforce the stability of the dam itself. Such nest dams allow the rapid flow of water while retard the fish, which affords beaver easy access to food. These structures modify the local environment and set up a comfortable ecosystem for beavers. Considering an electrochemical energy storage device with multi-electron chemistry, several basic requirements need to be satisfied for separators to achieve a cell with very high performance [9,10]: i) the separator should provide large quantities of anchoring sites to facilitate the adsorption and redox reaction of the intermediates generated from the active materials; ii) there should be abundant channels for rapid diffusion of ions as energy carriers in the electrolyte; iii) the structure of the separator should durable and robust for safe and persistent energy storage. Enlightened

* Corresponding authors.
E-mail addresses: jqhuang@bit.edu.cn (J.-Q. Huang), zhuwancheng@tsinghua.org.cn (W. Zhu), zhang-qiang@mails.tsinghua.edu.cn (Q. Zhang).
[1] These authors contributed equally to this work.

http://dx.doi.org/10.1016/j.ensm.2017.05.009
Received 20 April 2017; Received in revised form 11 May 2017; Accepted 11 May 2017
Available online 14 May 2017
2405-8297/ © 2017 Elsevier B.V. All rights reserved.

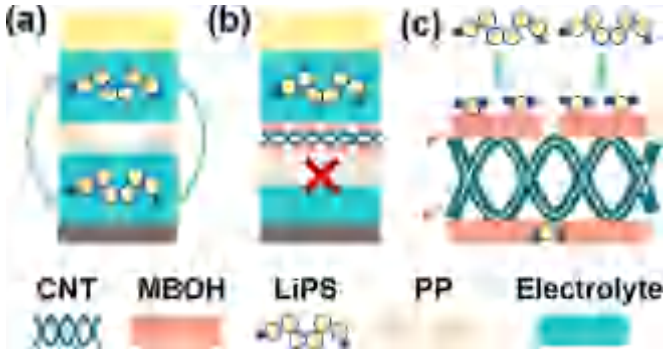

Fig. 1. The concept of nest separator for Li–S batteries. (a) LiPS shuttle in a routine Li–S cell with PP separator. (b, c) CNT/MBOH nest layer can retard the shuttle of LiPS and facilitate redox kinetics in a Li–S cell with nest separator.

by structure engineering of beaver dams in nature, a nest nanostructure is expected to be highly efficient in the intermediate adsorption and conversion, the rapid ion/electron transfer, and the structural stability.

Inspired by the structure of beaver dams, we herein propose the concept of self-assembly of hierarchical nest membranes and evaluate their applications in lithium–sulfur (Li–S) batteries [11]. We select the Li–S battery as the model system due to its very high energy density of 2600 W h kg^{-1}, affordable cost, natural abundance, and environmental benignity of the sulfur active materials [12–17]. However, the dissolution of lithium polysulfides (LiPS) during the multi-electron electrochemistry of Li–S system induces the notorious shuttle effect of LiPS in the whole system (Fig. 1a). The regulation of LiPS diffusion and conversion have been proposed by the rational design of cathode materials [18–21], but the complex behaviors of LiPS conversion are not thoroughly understood. The use of multi-functional separator/interlayer have also been pioneered by Manthiram [22–25], Cheng [26,27], and several research groups [28–40] for retarding LiPS migration. The polymer electrolytes with both high lithium transference number and ionic conductivity were considered for Li-S batteries

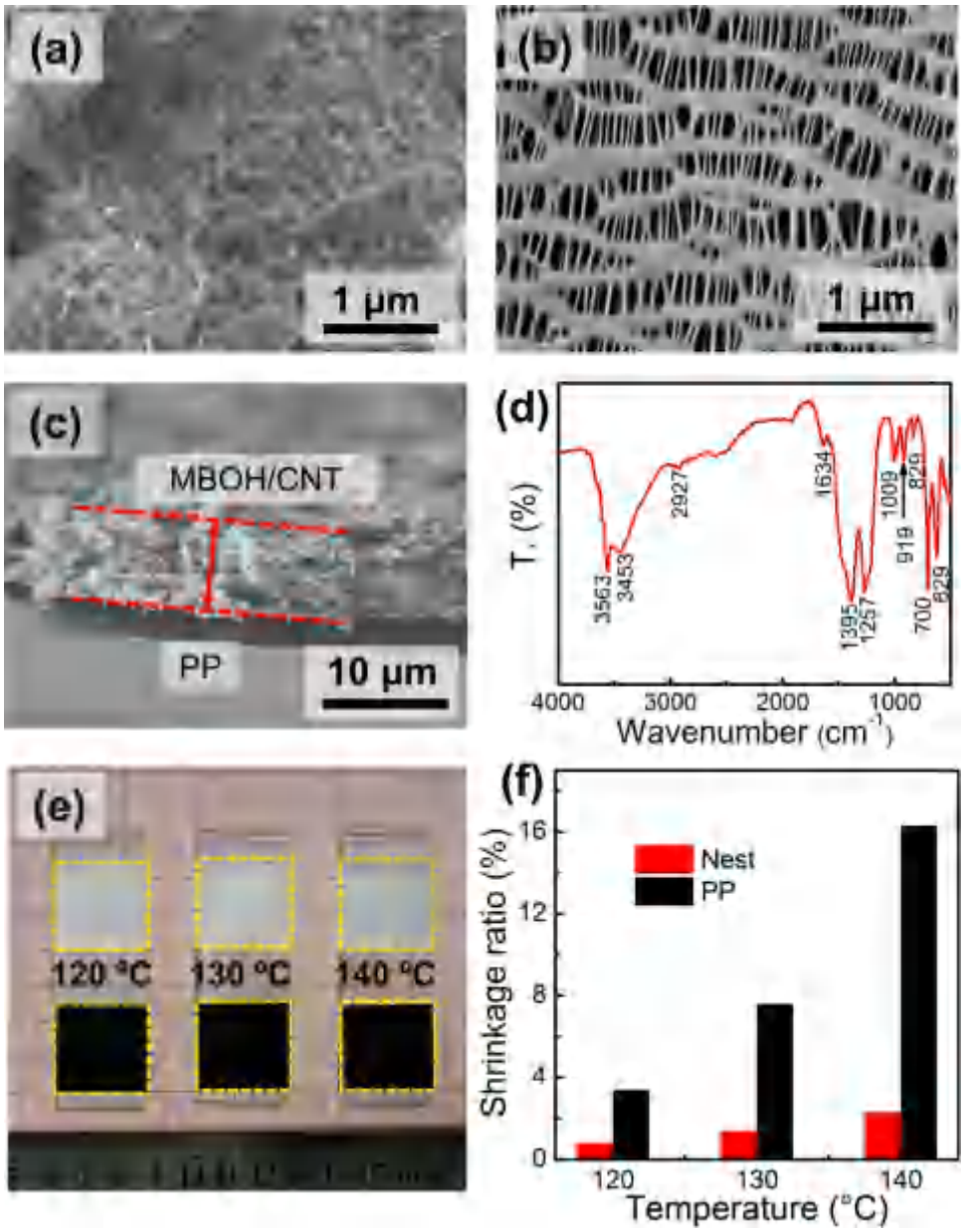

Fig. 2. SEM images of (a) nest and (b) PP separators. (c) Cross-sectional image of nest separator. (d) FT-IR spectrum of MBOH. (e) Thermal stability of nest and PP separators. (f) Shrinkage ratio of nest and PP separators.

[41–43]. However, the intrinsic insulating nature of sulfur and the complex energy chemistry of LiPS advocate a further optimized design of cell configurations with smart material architectures and capability of manipulating the local environments for favorable electrochemical behavior of sulfur and its intermediates.

In this contribution, a nest separator, integrated by an insulate polyproylene (PP), a highly electrical conducting network of carbon nanotubes (CNTs) and a LiPS-suppressing adsorbent of magnesium borate hydroxide ($MgBO_2(OH)$, abbreviated as MBOH) nanofibers, have been proposed (Fig. 1b). Mimicking the hierarchical structure of beaver dams that regulates water flow and controls natural flood, the interconnected ion channels in the nest membrane allow the diffusion of lithium ions, while inundant LiPS 'flood' are expected to be effectively blocked by the sulphifilic host, where the conversion of LiPS is simultaneously promoted. In details, MBOH nanofibers have been selected as the sulphifilic host for the chemical absorption and enhancement of the redox reaction of LiPS intermediates. CNTs are employed as conductive pathway to allow the transportation of electrons to facilitate the redox reaction of LiPS. The PP matrix, together with flexible CNTs and rigid MBOH nanofibers render the composite membrane robust and durable mechanical properties. In fact, the MBOH have drawn significant attention due to its perfect compatibility of low density, high mechanical strength [44], which is widely applied for composite reinforcement and widely available translucent mineral in nature [45]. Moreover, MBOH has low thermal expansion coefficient to withstand the mechanical stress induced by high temperature, consequently benefiting the battery safety. Besides, the large surface area, adequate functional groups (O^{2-}, −OH), and unique one dimensional (1D) nanofiber structure of MBOH expose sufficient chemical sites that may anchor LiPS through chemical adsorption (Fig. 1). Owing to rational engineering of nest nanostructure and synergistic attributes of MBOH and CNTs, the Li–S cell employing the well-designed separator demonstrated remarkable cycling stability and rate capability in comparison with routine cell with PP separator, as well as enhanced structural stability at elevated temperature.

2. Results and discussion

As shown in Fig. 2a, the 1D curved CNTs in designed nest separator act as branches of beaver dam to allow fast Li^+ transport. The rigid bamboo-leaf-like MBOH nanofibers serve as stones to reinforce the mechanical structure of functional layers and block the flooding of LiPSs through chemical absorptivity of LiPS intermediates.

The bamboo-leaf-like MBOH nanofibers were prepared by a facile hydrothermal method [46]. All peaks in the X-ray diffraction (XRD) pattern of the as-obtained nanofibers were assigned to $MgBO_2(OH)$ (PDF No. 39-1370) (Fig. S1, Supporting information). However, the peak position is slightly shifted toward low angle, which indicates the enlarged lattice distance in the MBOH nanofibers. The enlarged lattice distance was owing to the inferior crystallinity of MBOH through the low temperature hydrothermal synthesis.

The MBOH nanofibers with a diameter of 100–200 nm and a length of 1–2 μm were observed from scanning electron microscopy (SEM) and transmission electron microscopy (TEM) image (Fig. S2). The porosity of MBOH nanofibers and CNTs were probed by N_2 isotherms (Fig. S3a). A type-II isotherm with H3 hysteresis was detected for MBOH. The pore size distributions of MBOH were calculated based both density functional theory (DFT) and Barrett-Joyner-Halenda (BJH) models (Fig. S3b, c). The meso/macropores of MBOH are mainly derived from crosslinked nanofibers. The specific surface area of MBOH is calculated to be 103 $m^2 g^{-1}$, which affords the exposure of many active sites to anchor LiPS intermediates. The CNTs exhibit a similar isotherm and pore size distributions (Fig. S4). These were attributed to the similar morphologies of CNTs and MBOH nanofibers. The specific surface area of CNTs was calculated to be 235 $m^2 g^{-1}$.

After depositing MBOH/CNTs onto a routine PP separator, the coating side of PP became black (Fig. S5a). As shown in SEM images presented in Fig. 2a, b, intercrossed MBOH nanofibers and CNTs were observed on the black side, while the typical slit pores of PP were detected on the white PP side. The composite membrane is flexible and bendable (Fig. S5b, c). No obvious detachment of the coating layer was observed after repeated folding, indicating a highly durable mechanical structure. The uniform distribution of MBOH and CNTs fully enabled the synergy of electrical conductivity and chemisorptivity. In contrast, the routine PP separator with 200 nm slit pores across the whole area (Fig. 2b) accounts for the severe LiPS migration upon cycling [47]. The deposited functional nest layer was estimated to possess a thickness of ca. 7 μm (Fig. 2c). Such functional layer pillared by CNTs was anticipated to afford sufficient channels for rapid Li^+ transport, which was essentially important to achieve rapid redox kinetics, leading to an impressive capacity at a high current density.

The Fourier transform infrared spectroscopy (FT-IR) spectra of the nest separator was performed to identify molecule structure and chemical composition of functional layers (Fig. 2d). The characteristic peaks of $MgBO_2(OH)$ at 1634 cm^{-1} (bending of H–O–H), 1395 cm^{-1} (asymmetric stretching of $B_{(3)}$–O), 1257 cm^{-1} (in-plane bending of B–O–H), 1009 cm^{-1} (asymmetric stretching of $B_{(4)}$–O), 829 cm^{-1} (symmetric stretching of $B_{(4)}$–O), 700 cm^{-1} (out-of-plane bending of $B_{(3)}$–O) and 629 cm^{-1} (symmetric pulse vibration of $[B_2O_4(OH)_2]^{4-}$) were observed [48].

A strong and robust separator at elevated temperature plays a crucial role in practical use to avoid internal short circuits in a working battery for safety concerns. Herein both the nest and PP separator were laid at various temperatures ranging from 120 to 140°C for half an hour. The conspicuous shrinkage of routine PP separator was effectively alleviated by coating the functional MBOH/CNT nest (Fig. 2e). Fig. 2f quantitatively manifested the shrinkage ratio of PP and nest separators. Especially, the thermal shrinkage of routine separator was approximately 16.3% under 140°C, seven times higher than that of nest separator (2.3%). The superior thermal stability of the nest separator is attributed to the low thermal expansion coefficient of MBOH.

To clarify the intrinsic interfacial affinity between MBOH and LiPS, a visualized macroscopic adsorption test of LiPS was conducted by dispersing CNTs and MBOH in Li_2S_6 solution, respectively. A lucid solution with MBOH additive was observed (Fig. 3a), demonstrating the strong chemisorptivity of MBOH toward LiPS. The rich polar groups on MBOH surface, such as O^{2-} and −OH groups, served as the main anchoring sites. Even with a short adsorption period of 5 min (Fig. S6), the strong absorptivity of MBOH still ensured the rapid decoloration of LiPS solution. In contrast, CNTs possess weak interaction with LiPS, which is unfavorable for LiPS anchoring in long-term operation of Li–S cells.

To quantitatively describe the strong anchoring of LiPS in a working cell, the shuttle current of LiPS was recorded through a dynamic measurement [49,50]. The shuttle currents were recorded with $LiNO_3$ free electrolyte, which commonly led to severe crossover of LiPS. As shown in Fig. 3b, the shuttle current curve of the cell with a PP separator exhibited a sharp peak between 2.3 and 2.5 V, which was corresponding to the potential window of LiPS formation. The largest shuttle current of 0.43 mA cm^{-2} was detected at a charging voltage of 2.38 V. On the contrary, shuttle currents of the cell with a nest separator displayed tiny changes, revealing the significant advantage of MBOH in mitigating the diffusion of LiPS.

The stepwise reduction of sulfur from soluble LiPS to insoluble Li_2S_2/L_2S in ether-based electrolyte inevitably goes through typical nucleation and growth, which is strongly regulated by the interfacial affinity and the redox kinetics of LiPS. A reasonable interfacial affinity coupled with superb conductivity that favor the nucleation and growth afforded the feasibility to achieve high reversible capacity even at a high current density. The nucleation of $Li_2S_{(1/2)}$ was in-situ monitored to probe the multi-electron, phase-conversion chemistry in Li–S cells with

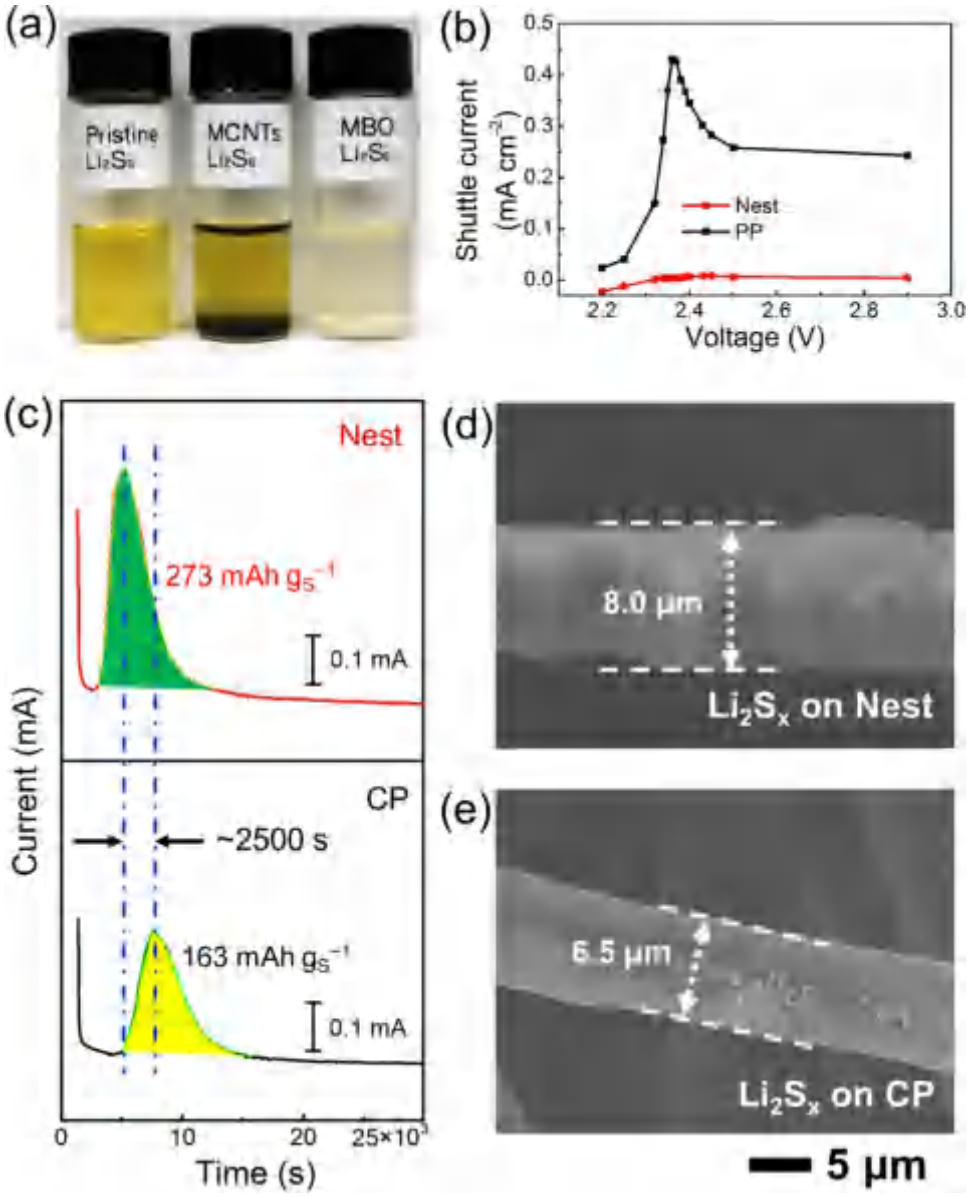

Fig. 3. Interfacial affinity between MBOH and LiPS. (a) Static adsorption of Li_2S_6 after 4 h. (b) The shuttle currents of Li–S cells with nest and PP separator versus applied charging voltages. (c) Potentiostatic discharge profiles of Li_2S_8/tetraglyme solution at 2.05 V on surface of nest separator and CP. The peak area filled with green and yellow colors indicates the amount of precipitation of Li_2S_x on surfaces of Nest and CP, respectively. (d) and (e) SEM images showing precipitation of Li_2S_x after 7000 s as indicated in panel (c). The scale bar is the same as indicated in the bottom right.

different separators. The commercial carbon paper (CP) and MBOH/CNTs loaded on CP (donated as nest) were employed for Li_2S_x nucleation according to previous reported methods [50–52]. Of note, the potentiostatic current with a nest interface reached its peak ca. 2500 s ahead in comparison with that of pristine CP, illustrating favorable nucleation condition on nest interface (Fig. 3c). This is originated from the adequate chemical sites that promotes strong interactions between LiPS and MBOH, and the rapid electron supply through the MBOH/CNT boundary. Based on the modeling proposed by Chiang and co-workers [51], the quantity of Li_2S_x precipitation was calculated to further distinguish interfacial contributions in the Li_2S_x nucleation process. Peak area integral of currents were 273 and 163 mA h g^{-1} on nest and PP interfaces, respectively.

Aiming at understand of catalyzed Li_2S nucleation and growth, the cathode was further observed by SEM to characterize the Li_2S precipitation (Fig. 3d and e) after ca. 7000 s potentiostatic discharge. After the Li_2S deposition, CP surface with nest components exhibited full-coverage deposits, which was distinct from a scattering nanofiber/nanotube deposition onto pristine CP (Fig. S7). An increased diameter of ca. 8 μm was detected, much larger than pristine of 5–6.5 μm. On the contrary, CP was only partially covered by several isolated two-dimensional islands (Fig. 3d), suggesting the weak affinity between nonpolar CP and polar LiPS molecules. These evidences that the favorable interfacial affinity coupled with conductive backbone possesses an enhanced capability to regulate the kinetic behavior of LiPS conversion on the sulphifilic surface of MBOH.

The nanostructured nest separator with MBOH/CNT components affords superb electrical conductivity for electron transport and favorable interfacial affinity toward LiPS intermediates. The cyclic voltammetry (CV) of a Li–S cell with a nest separator presented a typical two-step reduction reactions behavior (Fig. S8). The cathodic peaks at 2.3 and 2.0 V were detected in cathodic sweep. The higher cathodic peak represents transformation from S to long-chain LiPS (Li_2S_x, $3 \le x \le 8$). The lower cathodic peak at 2.0 V indicates the further reduction of long-chain LiPS to short-chain LiPS ($Li_2S_{(1/2)}$). The anodic peaks at 2.3 and 2.4 V correspond to reverse reactions from short-chain LiPS to S

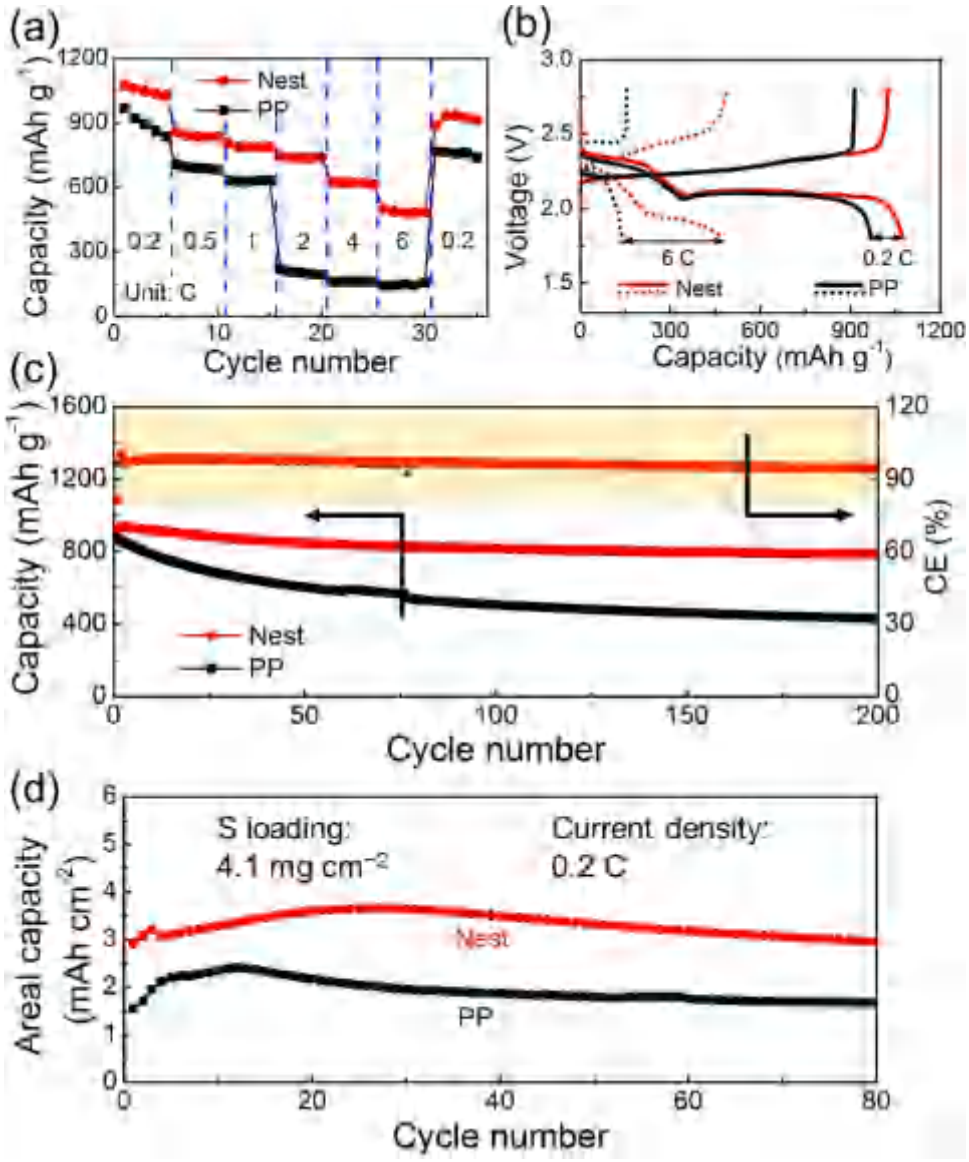

Fig. 4. Electrochemical performances of Li–S cells with Nest and PP separators. (a) The rate performance of Li-S batteries with Nest and PP separators (1 C=1672 mA g^{-1}). (b) Galvanostatic discharge–charge profiles at various current densities. (c) Long-term cycling performance at a current density of 0.5 C. The sulfur loading in panels (a–c) was 1.1 mg cm^{-2}. (d) Cycling performance of high-energy batteries with a high sulfur loading of 4.1 mg cm^{-2}.

through long-chain LiPS. Especially, the occurrence of two peaks in anodic process is quite distinct from previous reports [24,36,37,39], in which only one anodic peak was identified. Normally, the oxidation of solid LiPS ($Li_2S_{(1/2)}$) has to overcome high energy barrier because insulating nature of solid LiPS, which leads to remarkable over-potential. Consequently, a broad anodic peak that represents solid and liquid LiPS conversion is achieved. In this contribution, two anodic peaks were observed in CV profile, indicating excellent kinetic features of LiPS redox reaction.

The superiority of the nest separator was demonstrated by cycling cells at various current densities (Fig. 4a). The sulfur/carbon cathode with an areal sulfur loading of 1.1 mg cm^{-2} and a sulfur content of 70% manifested a discharge capacity of 1074 mA h g^{-1} at 0.2 C in a cell with a nest separator. With further increasing current densities to 0.5, 1, 2, 4, and 6 C, the cell with nest separator achieved high reversible discharge capacities of 859, 803, 747, 624, and 500 mA h g^{-1}, respectively. A high capacity of 933 mA h g^{-1} was resumed after shifting current density back to 0.2 C. However, the capacity of the cell with a PP separator dropped sharply from 632 to 219 mA h g^{-1} when the current density increased from 1 to 2 C, indicating a sluggish kinetics of LiPS redox reactions in a cell with routine PP separator.

The electrochemical impedance spectroscopy (EIS) of the cells with various nest and PP separators were recorded after the initial cycle at 2.3 V in charged state (Fig. S9). The smaller diameter of semicircle of the cell with a nest separator demonstrated a reduced charge transfer resistance while the steeper straight line was attributed to the rapid diffusion of Li^+ in the electrode. This ensured much enhanced rate capability of the Li–S cells with nest membranes. The Li^+ transference number of PP and nest separator are 0.403 and 0.428, respectively. The abrupt drop in capacity for the routine cell is explained by discharge curves in Fig. 4b. The high applied current density has a significant effect on the second plateau, corresponding to the formation of electronically insulating layers of Li_2S_2/L_2S. The insufficient electron transport pathways and unfavorable bindings of LiPS to conductive surface result in the disappearance of second plateau, which ultimately accounts for the rapid decline of discharge capacity for the cell with a routine PP separator. On the contrary, the integration of MBOH in CNTs affords nanoscale local environment to anchor LiPS intermediates and accelerate the redox reaction of LiPS, which otherwise migrated to anode or easily evolved to ‘dead sulfur’ in the subsequent

cycling due to detachment from conductive framework [36,53–57]. The continuous interconnected functional layer in a nest separator renders long-distance yet express paths for electron transport and ion diffusion channels across the cell, enabling exceptionally high rate performance.

Apart from the superb rate capability, Li–S cells with nest separators also demonstrated high stability in long cycles (Fig. 4c). The reversible discharge capacity of the cell with a nest separator displayed an initial capacity of 924 mA h g^{-1} at 0.5 C. After 200 cycles, a discharge capacity of 785 mA h g^{-1} was preserved, corresponding to a cyclic decay rate of 0.075%. The cell with a PP separator delivered a similar initial discharge capacity of 872 mA h g^{-1} but only maintained a discharge capacity of 430 mA h g^{-1} after 200 cycles, which corresponded to a large capacity decay rate of 0.25% per cycle.

The nest separator with the function of retarding LiPS was further demonstrated with a $LiNO_3$-free electrolyte (Fig. S10). Other control cells with routine PP, CNT/PP, and MBOH/PP separator were also tested. The cell with a nest separator exhibited the best cycling performance both in discharge specific capacity and Columbic efficiency (CE) (Fig. S10a, b). In contrast, the cell with CNTs on separator exhibited higher initial discharge capacity of 1028 mA h g^{-1}, but a more rapid capacity decay than that of nest separator. This is ascribed to insufficient interfacial affinity to LiPS, which has been proved by the macroscopic visual absorption shown in Fig. 3a. In addition, the cell with MBOH coating presented improved cycling stability in comparison with the cell with a PP separator, even comparable to the cell with CNTs in terms of capacity retention (as indicated in Fig. S10a). However, the intrinsic insulating nature of MBOH cannot afford facilitated interfacial charge transfer, which was unfavorable for the subsequent redox kinetics of adsorbed active molecules and eventually induced low capacity. Moreover, the CE of the cell with a nest separator was approximately 90% after 100 cycles, much higher than that of routine PP separator (~76%) (Fig. S10b). The higher CE ultimately render the enhanced cycling stability than cells with PP, CNT/PP, and MBOH/PP separator.

The nest separators also exhibit an advantage in its compatibility with sulfur cathodes with a high areal loading. Fig. 4d exhibited the cyclic performance of a cathode with a sulfur loading at 4.1 mg cm^{-2} and a nest separator. The areal capacity of nest-separator-based cell delivered an initial reversible capacity of 2.91 mA h cm^{-2} at a high current density of 0.2 C. A slight increase of discharge capacities in the initial several cycles originated from gradual activation induced by the long electron/ion diffusion distance across thick electrodes coupled with a re-distribution of sulfur active materials. Thereafter, the capacity became stable and displayed a bit decay upon extended cycling. In contrast, the Li–S cell with a PP separator afford a lower capacity of 1.55 mA h cm^{-2}, and remained almost half of the nest separator cell. The nest separator endowed a Li–S cell with high rate capability, long cycle stability, and improved sulfur utilization.

To better understand the role of the nest separator in a Li–S battery, Li–S cells were disassembled and elaborately examined by postmortem analysis in the charged state after 10 cycles (Fig. 5). The yellow precipitates were observed on the cathode side of PP separator in the whole area, indicating the flooding of LiPS in a working cell. The nest separator exhibited a black color probably owing to the coverage of sulfur by the functional nest layer (Fig. 5a). Surprisingly, the digital pictures of separators in anode side exhibited the distinct changes (Fig. 5b) when a nest layer was applied. The sulfur-containing species were well-confined in the circled area, indicating the strong capability to localize the flooding of LiPS. Such a capability surprisingly mimic the natural role of beaver dams in controlling floods of LiPS intermediates.

To check the distribution of the sulfur species in a Li–S cell, the morphology of the nest and PP separator facing sulfur cathode and lithium anode were observed by SEM. The functional MBOH/CNT layer was fully filled by sulfur (Fig. 5c) in the cathode of a nest cell, which indicated the efficient entrapment of LiPS by the synergistic effects from chemical affinity contributed by MBOH and LiPS. This endowed the nest with ideal ability as a 'dam' to obstruct flood of LiPS during the charge and discharge processes of a working Li–S cell. In contrast, the readily diffused LiPS abruptly distributed and consequently deposited on the routine PP separator in the charge process (Fig. 5d). The deposited sulfur with no accessibility to a conductive matrix can hardly participate redox reactions, which ultimately induced the rapid decay of discharge capacity. More importantly, the 'dead sulfur' covered on PP also severely blocked the pathways for Li^+ diffusion, detrimentally degrading the rate capability of Li–S batteries. This is one reason for poor rate performance shown in Fig. 4a. Fig. 5e, f presented SEM observations of nest and PP separators in anode side, respectively. The effectively retarding LiPS enabled by MBOH promised the clean surface of separator in contact with lithium anode (Fig. 5e). As a result, the undesirable side reactions at the anode surface are also implied. However, the leakage of LiPS through the slit pores of PP upon cycling resulted in acceleration of deposits and finally evolved in a number of heaps (Fig. 5f).

The chemical compositions of cathode, separator (cathode side), and anode were further probed by ex-situ Raman spectroscopy (Fig. 5g) at charged state after 10 cycles. Three major peaks at 152, 218, and 470 cm^{-1} were indexed to elemental sulfur while other predominant resonances were ascribed to LiPS with various formulas [58]. At cathode side, the elemental sulfur was dominated for a nest cell due to the nearly complete oxidation of LiPS enabled by the superb electrical conductivity and improved redox kinetics of the MBOH/CNT nest, whereas LiPS can still be detected in the cathode of a PP cell, suggesting the incomplete conversion. This validated the advantages of the nest separator to favor the full utilization of sulfur cathode. On the separator, the Raman spectra of the nest cell exhibited less conspicuous sulfur signals than that of the PP cell, which was attributed to the less probability for LiPS passing through and precipitating in the nest separator. While the strong sulfur peaks indicated the accumulation of LiPS diffusion across the PP separator and followed by transforming to sulfur. The close examination of the anode of a PP cell in 325 cm^{-1} revealed onset reactions between LiPS and lithium while the absence of resonances was identified in anode of nest cell, demonstrating much less migration of LiPS toward Li metal anode. The morphology evolution of Li anode in Li–S cells with nest and PP separators were observed by SEM after 200 cycles and shown in Fig. S11. The Li corrosion in a Li–S cell with a PP separator was much severe over that of a nest separator. This can be directly stemmed from the huge LiPS migration through pores of PP, which was considerably alleviated through a nest separator.

The excellent rate and cycling performance of the Li–S cell with a beaver-dam-like MBOH/CNT/PP separator are ascribed to the hierarchical structure of the nest membranes. Compared with routine polymer membrane, the beaver-dam-like separator affords a robust and sulphifilic nest to allow the rapid diffusion of Li^+ ions and effective absorb the LiPS intermediates. The MBOH nanofibers with polar surfaces exhibit strong affinity to polar polysulfides, which is similar to other oxides [18,59], nitrides [60], sulfides [61–63], hydroxides [50,64], and heteroatoms/functional groups in carbon materials [65,66] that can entrap the intermediates into the porous separator. The nucleation of $Li_2S_{(1/2)}$ is therefore enhanced, which is strongly supported by the potentiostatic current measurement. The shuttle current of a working cell with a nest separator was significantly reduced. Furthermore, the addition of CNTs afford 3D interconnected electron pathways, which can reutilize the absorbed LiPS during charging process [36,53–57,67]. The synergy between MBOH and CNTs avoids the loss of active materials in form of electrical isolated phases and minimize the notorious shuttle of polysulfides, which not only enhanced the sulfur utilization and rate performance, but also extended the life of a Li–S cell through the effective regulation of LiPS shuttle and suppression of anode corrosion induced by LiPS intermediates [68–70]. The beaver-dam-like MBOH/CNT separator also exhibits a robust mechanical/thermal stability at a very high temperature up to 140 °C, which is quite promising for high-temperature cell without separator shrinkage and therefore increase the safety of a working cell. As a result, the bio-inspired nest membrane can serve as much better separator for Li–S batteries than routine polymer separator.

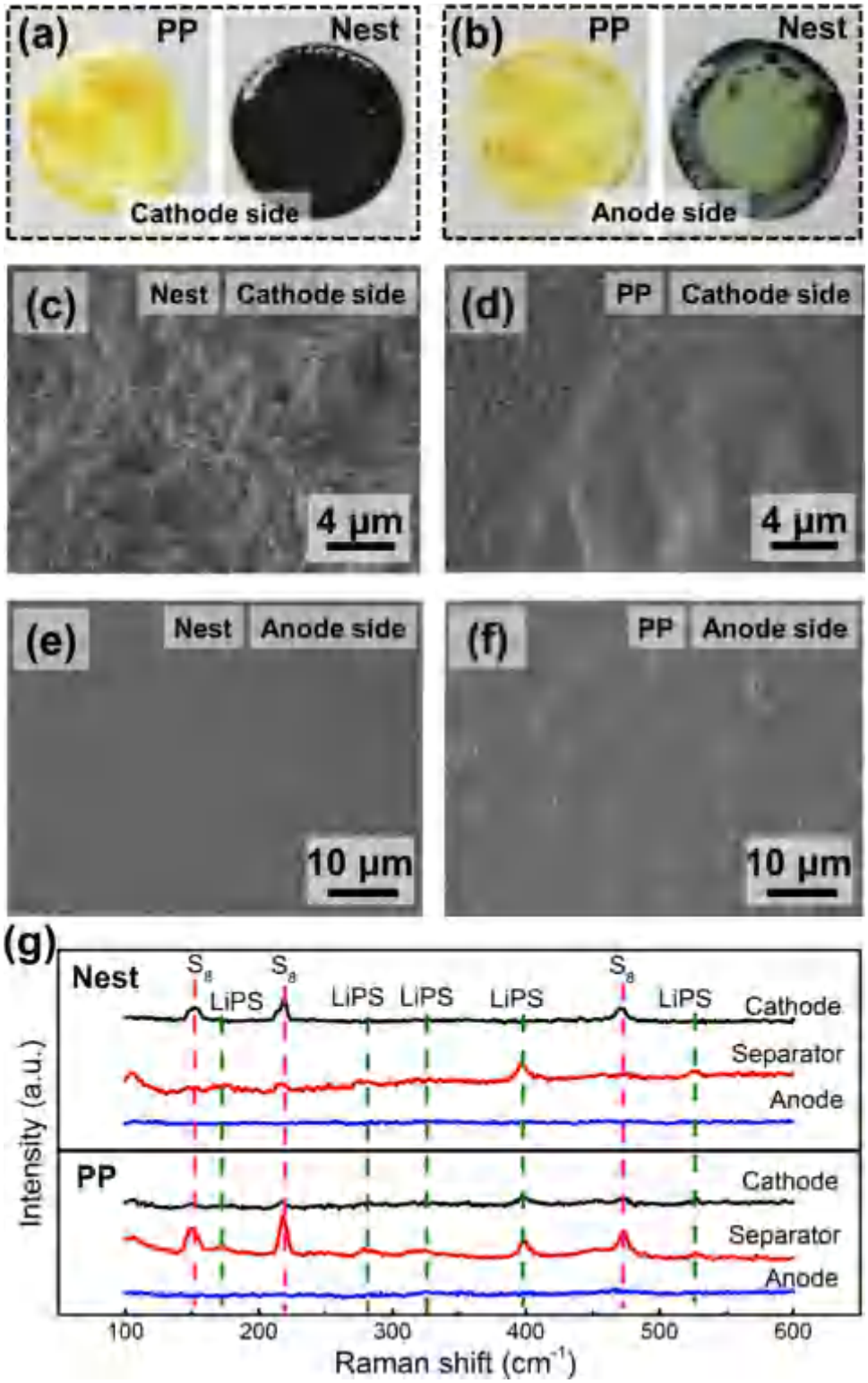

Fig. 5. Morphology and composition of cycled separators after 10 cycles at charged state. Digital image of cycled nest and PP separator on (a) cathode and (b) anode sides, respectively. SEM images of (c) nest, (d) PP separators on cathode sides and (e) nest, (f) PP separators on anode sides. (g) Raman spectra of cycled Li–S cells with nest and PP separators.

3. Conclusions

We fabricated a beaver-dam-like MBOH/CNT/PP nest separator for lithium sulfur batteries with high sulfur utilization, high rate retention, and excellent cycling performance. The hybrid nanostructure of functional layers was integrated by an electrical conducting CNT network and rigid MBOH nanofibers, showing synergistic advantages in robust mechanical stability, rapid lithium ion transport, inhabitation of polysulfide flooding, and rapid redox kinetics. The sulphifilic MBOH nanofibers possessed intriguing capability to absorb LiPS intermediates and enhance the nucleation of $Li_2S_{(1/2)}$. Consequently, the adverse shuttle effect was effectively retarded in a Li–S cell with a nest separator. The interconnected CNT conductive framework facilitated express pathways for electron transport. The smart construction of

MBOH and CNTs with their synergistic attributes consequently rendered long cycling stability of 785 mA h g^{-1} after 200 cycles, high rate capability of 500 mA h g^{-1} at 6 C, enhanced areal capacity of 2.91 mA h cm^{-2}, and improved thermal stability. The presented design enlightened by beaver dam shed light on engineering novel separator in terms of enhanced thermal stability and desired chemisorptivity enabled by MBOH, as well as the synergy originated from CNTs with superb electrical conductivity and robust scaffolds. This bio-inspired concept can be further extended to design multifunctional separator for other battery systems with multi-electron chemistry for advanced energy storage.

Acknowledgements

This work was supported by National Key Research and Development Program (Nos. 2016YFA0202500 and 2016YFA0200102), Natural Scientific Foundation of China (Nos. 21676160, 21276141, and 21561130151), and CAS Key Laboratory of Carbon Materials (No: KLCMKFJJ1701). We thank Ying-Zhi Sun, Xiang Chen, and Chong Yan at Tsinghua University for helpful discussion.

Appendix A. Supplementary material

Supplementary data associated with this article can be found in the online version at doi:10.1016/j.ensm.2017.05.009.

References

[1] M.Q. Zhao, Q. Zhang, J.Q. Huang, F. Wei, Adv. Funct. Mater. 22 (2012) 675–694.
[2] T. Chen, B. Cheng, G. Zhu, R. Chen, Y. Hu, L. Ma, H. Lv, Y. Wang, J. Liang, Z. Tie, Z. Jin, J. Liu, Nano Lett. 17 (2017) 437–444.
[3] T. Zhao, Y. Ye, X. Peng, G. Divitini, H.K. Kim, C.Y. Lao, P.R. Coxon, K. Xi, Y.J. Liu, C. Ducati, R.J. Chen, R.V. Kumar, Adv. Funct. Mater. 26 (2016) 8418–8426.
[4] W.Y. Li, Z.Y. Zhang, W.P. Kang, Y.B. Tang, C.S. Lee, ChemElectroChem 3 (2016) 999–1005.
[5] H. Li, L.P. Sun, G.C. Wang, ACS Appl. Mater. Interfaces 8 (2016) 6061–6071.
[6] Z. Li, J.T. Zhang, Y.M. Chen, J. Li, X.W. Lou, Nat. Commun. 6 (2015) 8850.
[7] S.Y. Yuan, Z.Y. Guo, L.N. Wang, S. Hu, Y.G. Wang, Y.Y. Xia, Adv. Sci. 2 (2015) 1500071.
[8] M.Q. Zhao, H.J. Peng, G.L. Tian, Q. Zhang, J.Q. Huang, X.B. Cheng, C. Tang, F. Wei, Adv. Mater. 26 (2014) 7051–7058.
[9] J.Q. Huang, Q. Zhang, F. Wei, Energy Storage Mater. 1 (2015) 127–145.
[10] N.P. Deng, W.M. Kang, Y.B. Liu, J.G. Ju, D.Y. Wu, L. Li, B.S. Hassan, B.W. Cheng, J. Power Sources 331 (2016) 132–155.
[11] R. Fang, S. Zhao, Z. Sun, D.-W. Wang, H.-M. Cheng, F. Li, Adv. Mater. 29 (2017) 1606823.
[12] A. Manthiram, S.H. Chung, C. Zu, Adv. Mater. 27 (2015) 1980–2006.
[13] Y.X. Yin, S. Xin, Y.G. Guo, L.J. Wan, Angew. Chem. Int. Ed. 52 (2013) 13186–13200.
[14] J. Liang, Z.-H. Sun, F. Li, H.-M. Cheng, Energy Storage Mater. 2 (2016) 76–106.
[15] J.G. Wang, K.Y. Xie, B.Q. Wei, Nano Energy 15 (2015) 413–444.
[16] H.-J. Peng, J.-Q. Huang, X.-B. Cheng, Q. Zhang, Adv. Energy Mater. 7 (2017) 1700260.
[17] R.P. Fang, S.Y. Zhao, Z.H. Sun, D.W. Wang, H.M. Cheng, F. Li, Adv. Mater. 29 (2017) 1606823.
[18] X.Y. Tao, J.G. Wang, Z.G. Ying, Q.X. Cai, G.Y. Zheng, Y.P. Gan, H. Huang, Y. Xia, C. Liang, W.K. Zhang, Y. Cui, Nano Lett. 14 (2014) 5288–5294.
[19] X.Y. Tao, J.G. Wang, C. Liu, H.T. Wang, H.B. Yao, G.Y. Zheng, Z.W. Seh, Q.X. Cai, W.Y. Li, G.M. Zhou, C.X. Zu, Y. Cui, Nat. Commun. 7 (2016) 11203.
[20] Z.W. Seh, Y.M. Sun, Q.F. Zhang, Y. Cui, Chem. Soc. Rev. 45 (2016) 5605–5634.
[21] L. Borchardt, M. Oschatz, S. Kaskel, Chem. Eur. J. 22 (2016) 7324–7351.
[22] S.H. Chung, P. Han, R. Singhal, V. Kalra, A. Manthiram, Adv. Energy Mater. 5 (2015) 1500738.
[23] S.H. Chung, A. Manthiram, Adv. Funct. Mater. 24 (2014) 5299–5306.
[24] S.H. Chung, A. Manthiram, Adv. Mater. 26 (2014) 7352–7357.
[25] C.H. Chang, S.H. Chung, A. Manthiram, Small 12 (2016) 174–179.
[26] G. Zhou, L. Li, D.W. Wang, X.Y. Shan, S. Pei, F. Li, H.M. Cheng, Adv. Mater. 27 (2015) 641–647.
[27] R.P. Fang, S.Y. Zhao, S.F. Pei, Y.X. Cheng, P.X. Hou, M. Liu, H.M. Cheng, C. Liu, F. Li, Carbon 109 (2016) 719–726.
[28] J.-Q. Huang, Q. Zhang, H.-J. Peng, X.-Y. Liu, W.-Z. Qian, F. Wei, Energy Environ. Sci. 7 (2014) 347–353.
[29] J.Q. Huang, T.Z. Zhuang, Q. Zhang, H.J. Peng, C.M. Chen, F. Wei, ACS Nano 9 (2015) 3002–3011.
[30] J.R. Nair, F. Bella, N. Angulakshmi, A.M. Stephan, C. Gerbaldi, Energy Storage Mater. 3 (2016) 69–76.
[31] N.Q. Liu, B.C. Huang, W.K. Wang, H.Y. Shao, C.M. Li, H. Zhang, A.B. Wang, K.G. Yuan, Y.Q. Huang, ACS Appl. Mater. Interfaces 8 (2016) 16101–16107.
[32] J.J. Song, D.W. Su, X.Q. Xie, X. Guo, W.Z. Bao, G.J. Shao, G.X. Wang, ACS Appl. Mater. Interfaces 8 (2016) 29427–29433.
[33] M. Shaibani, A. Akbari, P. Sheath, C.D. Easton, P.C. Banerjee, K. Konstas, A. Fakhfouri, M. Barghamadi, M.M. Musameh, A.S. Best, T. Ruther, P.J. Mahon, M.R. Hill, A.F. Hollenkamp, M. Majumder, ACS Nano 10 (2016) 7768–7779.
[34] T. Yim, S.H. Han, N.H. Park, M.S. Park, J.H. Lee, J. Shin, J.W. Choi, Y. Jung, Y.N. Jo, J.S. Yu, K.J. Kim, Adv. Funct. Mater. 26 (2016) 7817–7823.
[35] Y. Zhao, M. Liu, W. Lv, Y.B. He, C. Wang, Q.B. Yun, B.H. Li, F.Y. Kang, Q.H. Yang, Nano Energy 30 (2016) 1–8.
[36] J. Yoo, S.J. Cho, G.Y. Jung, S.H. Kim, K.H. Choi, J.H. Kim, C.K. Lee, S.K. Kwak, S.Y. Lee, Nano Lett. 16 (2016) 3292–3300.
[37] G.M. Zhou, Y.B. Zhao, C.X. Zu, A. Manthiram, Nano Energy 12 (2015) 240–249.
[38] J.D. Zhu, Y.Q. Ge, D. Kim, Y. Lu, C. Chen, M.J. Jiang, X.W. Zhang, Nano Energy 20 (2016) 176–184.
[39] J. Balach, T. Jaumann, M. Klose, S. Oswald, J. Eckert, L. Giebeler, Adv. Funct. Mater. 25 (2015) 5285–5291.
[40] P.-Y. Zhai, H.-J. Peng, X.-B. Cheng, L. Zhu, J.-Q. Huang, W. Zhu, Q. Zhang, Energy Storage Mater. 7 (2017) 56–63.
[41] L. Porcarelli, A.S. Shaplov, F. Bella, J.R. Nair, D. Mecerreyes, C. Gerbaldi, ACS Energy Lett. 1 (2016) 678–682.
[42] Y. Zhu, J. Li, J. Liu, J. Power Sources 351 (2017) 17–25.
[43] J.R. Nair, M. Destro, F. Bella, G.B. Appetecchi, C. Gerbaldi, J. Power Sources 306 (2016) 258–267.
[44] X.Y. Tao, X.D. Li, Nano Lett. 8 (2008) 505–510.
[45] L. Kumari, W. Li, S. Kulkarni, K. Wu, W. Chen, C. Wang, C.H. Vannoy, R.M. Leblanc, Nanoscale Res. Lett. 5 (2009) 149.
[46] W. Zhu, R. Wang, S. Zhu, L. Zhang, X. Cui, H. Zhang, X. Piao, Q. Zhang, ACS Sustain. Chem. Eng. 2 (2014) 836–845.
[47] T.Z. Zhuang, J.Q. Huang, H.J. Peng, L.Y. He, X.B. Cheng, C.M. Chen, Q. Zhang, Small 12 (2016) 381–389.
[48] J. Liu, S. Xia, S. Gao, Spectrochim. Acta A 51 (1995) 519–532.
[49] D. Moy, A. Manivannan, S. Narayanan, J. Electrochem. Soc. 162 (2015) A1–A7.
[50] H.J. Peng, Z.W. Zhang, J.Q. Huang, G. Zhang, J. Xie, W.T. Xu, J.L. Shi, X. Chen, X.B. Cheng, Q. Zhang, Adv. Mater. 28 (2016) 9551–9558.
[51] F.Y. Fan, W.C. Carter, Y.M. Chiang, Adv. Mater. 27 (2015) 5203–5209.
[52] H.J. Peng, G. Zhang, X. Chen, Z.W. Zhang, W.T. Xu, J.Q. Huang, Q. Zhang, Angew. Chem. Int. Ed. 55 (2016) 12990–12995.
[53] H. Yao, K. Yan, W. Li, G. Zheng, D. Kong, Z.W. Seh, V.K. Narasimhan, Z. Liang, Y. Cui, Energy Environ. Sci. 7 (2014) 3381–3390.
[54] J. Balach, H.K. Singh, S. Gomoll, T. Jaumann, M. Klose, S. Oswald, M. Richter, J. Eckert, L. Giebeler, ACS Appl. Mater. Interfaces 8 (2016) 14586–14595.
[55] Y.S. Oh, G.Y. Jung, J.H. Kim, J.H. Kim, S.H. Kim, S.K. Kwak, S.Y. Lee, Adv. Funct. Mater. 26 (2016) 7074–7083.
[56] S.A. Abbas, M.A. Ibrahem, L.H. Hu, C.N. Lin, J. Fang, K.M. Boopathi, P.C. Wang, L.J. Li, C.W. Chu, J. Mater. Chem. A 4 (2016) 9661–9669.
[57] H.J. Peng, D.W. Wang, J.Q. Huang, X.B. Cheng, Z. Yuan, F. Wei, Q. Zhang, Adv. Sci. 3 (2016) 1500268.
[58] M. Hagen, P. Schiffels, M. Hammer, S. Dörfler, J. Tübke, M. Hoffmann, H. Althues, S. Kaskel, J. Electrochem. Soc. 160 (2013) A1205–A1214.
[59] X. Liang, L.F. Nazar, ACS Nano 10 (2016) 4192–4198.
[60] Q. Pang, L.F. Nazar, ACS Nano 10 (2016) 4111–4118.
[61] Z. Yuan, H.-J. Peng, T.-Z. Hou, J.-Q. Huang, C.-M. Chen, D.-W. Wang, X.-B. Cheng, F. Wei, Q. Zhang, Nano Lett. 16 (2016) 519–527.
[62] A. Douglas, R. Carter, L. Oakes, K. Share, A.P. Cohn, C.L. Pint, ACS Nano 9 (2015) 11156–11165.
[63] Z.A. Ghazi, X. He, A.M. Khattak, N.A. Khan, B. Liang, A. Iqbal, J. Wang, H. Sin, L. Li, Z. Tang, Adv. Mater. 29 (2017) 1606817.
[64] J.T. Zhang, H. Hu, Z. Li, X.W. Lou, Angew. Chem. Int. Ed. 55 (2016) 3982–3986.
[65] J.X. Song, M.L. Gordin, T. Xu, S.R. Chen, Z.X. Yu, H. Sohn, J. Lu, Y. Ren, Y.H. Duan, D.H. Wang, Angew. Chem. Int. Ed. 54 (2015) 4325–4329.
[66] L. Ma, H.L.L. Zhuang, S.Y. Wei, K.E. Hendrickson, M.S. Kim, G. Cohn, R.G. Hennig, L.A. Archer, ACS Nano 10 (2016) 1050–1059.
[67] W. Kong, L. Yan, Y. Luo, D. Wang, K. Jiang, Q. Li, S. Fan, J. Wang, Adv. Funct. Mater. 27 (2017) 1606663.
[68] R.G. Cao, W. Xu, D.P. Lv, J. Xiao, J.G. Zhang, Adv. Energy Mater. 5 (2015) 1402273.
[69] C.-Z. Zhao, X.-B. Cheng, R. Zhang, H.-J. Peng, J.-Q. Huang, R. Ran, Z.-H. Huang, F. Wei, Q. Zhang, Energy Storage Mater. 3 (2016) 77–84.
[70] L. Qie, C.X. Zu, A. Manthiram, Adv. Energy Mater. 6 (2016) 1502459.